Journal of Magnetic Resonance 213 (2011) 90–97

Contents lists available at SciVerse ScienceDirect

Journal of Magnetic Resonance

journal homepage: www.elsevier.com/locate/jmr

High pressure magnetic resonance imaging with metallic vessels

Hui Han [a], Matthew Ouellette [a], Bryce MacMillan [a], Frederic Goora [a], Rodney MacGregor [a], Derrick Green [b], Bruce J. Balcom [a,*]

[a] MRI Centre, Department of Physics, University of New Brunswick, Fredericton, New Brunswick, Canada E3B 5A3
[b] Green Imaging Technologies, 2024 Lincoln Road, Fredericton, NB, Canada E3B 8M7

ARTICLE INFO

Article history:
Received 27 June 2011
Revised 25 August 2011
Available online 10 September 2011

Keywords:
High pressure MRI
Pressure vessel
Metallic pressure vessel
Rock core holder
Core flooding
Temperature control
Pressurized RF probe
Static B_0 field
Dynamic B_0 field
High pressure NMR

ABSTRACT

High pressure measurements in most scientific fields rely on metal vessels given the superior tensile strength of metals. We introduce high pressure magnetic resonance imaging (MRI) measurements with metallic vessels. The developed MRI compatible metallic pressure vessel concept is very general in application. Macroscopic physical systems are now amenable to spatially resolved nuclear magnetic resonance (NMR) study at variable pressure and temperature. Metallic pressure vessels not only provide inherently high tensile strengths and efficient temperature control, they also permit optimization of the MRI RF probe sensitivity. An MRI compatible pressure vessel is demonstrated with a rock core holder fabricated using non-magnetic stainless steel. Water flooding through a porous rock under pressure is shown as an example of its applications. High pressure NMR spectroscopy plays an indispensable role in several science fields. This work will open new vistas of study for high pressure material science MRI and MR.
© 2011 Elsevier Inc. All rights reserved.

1. Introduction

During the past half century high pressure NMR spectroscopy has played an indispensable role in diverse areas of physics and chemistry [1–6]. In particular, NMR measurements at high pressure provide unique information about the microscopic behavior of liquids [2,3]. MRI has revolutionized clinical diagnostic imaging and its use exploring and understanding natural science systems is expanding. There is clear merit in combining MRI with high pressure for materials investigation.

A limited number of high pressure MRI studies have been reported [7–10]. These studies employ non-metallic, mostly polymer composite, cells fit into an existing MRI RF probe. These measurements are hindered by inefficient temperature control due to low thermal conductivity of the polymer [8–10] and low sensitivity of the RF probe due to the distance between the probe and the sample under investigation [8–10]. Conventional (non-MR) laboratory studies at high pressure rely on metal vessels given the superior tensile strength of metals. The high thermal conductivity of metals makes them a natural choice for measurements at variable temperature.

We introduce high pressure magnetic resonance imaging using metallic vessels. The metallic vessel encloses a pressurized MRI RF probe with the metal enclosure functioning as an RF shield. The metallic pressure vessel, surrounded by a temperature control coil, fits inside a standard gradient bore on an MR spectrometer. In previous work [11], we have shown the eddy current problem associated with MR imaging inside highly conductive metallic structures may be solved by magnetic field gradient measurement and k-space data correction.

The metallic pressure vessels envisaged are very general in concept. They may be high pressure pipes, closed vessels of various designs or core holders with radial pressure application. In this article we choose a rock core holder as a simple example of a metallic pressure vessel. A core holder is employed to maintain the cylindrical rock sample at high pressure and specified temperature in order to recreate petroleum reservoir conditions. MR/MRI can be employed to analyze the fluid behavior in rock core samples to obtain information about the nature of the reservoir.

A core holder fabricated using non-magnetic stainless steel is demonstrated. The paper examines how the MRI measurement is altered when a large scale metal enclosure is introduced in a strong static B_0 magnetic field with a dynamic magnetic field gradient. As an illustration of its utility, water flooding a porous rock under pressure, confined in a metallic core holder, is monitored by MRI.

Gerald and coworkers [12] have undertaken MRI profiling in metallic vessels by employing spatially varying RF pulses for

* Corresponding author. Fax: +1 506 453 4581.
E-mail address: bjb@unb.ca (B.J. Balcom).

1090-7807/$ - see front matter © 2011 Elsevier Inc. All rights reserved.
doi:10.1016/j.jmr.2011.09.001

spatial encoding. This strategy is limited in its utility because it does not employ switched magnetic field gradients, which are essential to advanced MR/MRI measurements [13,14].

2. Methods and materials

2.1. MRI compatible metallic pressure vessels

Fig. 1a shows a schematic of high pressure MRI with metallic vessels. The MRI RF coil is integrated inside a metallic cell that is constructed using non-magnetic metal alloys. The high tensile strength of metals permits larger macroscopic volumes to be studied by MRI. As the size of a pressure cell increases, the required yield strength of the cell must increase proportionally to maintain the same maximum pressure. For a thin walled cylindrical pressure vessel [15], the stress is

$$\sigma_\theta = \frac{pr}{d} \tag{1}$$

where σ_θ is stress in the circumferential direction, p is the pressure difference from ambient pressure, r is the inner radius of the cylinder, while d is the thickness of the wall. The high yield strength of stainless steel makes it a near universal choice for conventional pressure vessels. A variety of metals may be employed for fabricating the cylindrical vessel including aluminum, non-magnetic stainless steel, brass and titanium. The physical properties relevant to MRI compatible pressure vessels are shown in Table 1 [16,17]. Stainless steel has a very high tensile strength of 400 MPa [16], twice that of aluminum.

Fig. 1b depicts a core holder embodying the principles outlined in Fig. 1a. The metallic outer case encloses an MRI probe that in turn contains a sample. Two metal disk-like end plugs are threaded into the outer case. O-rings provide a pressure seal on each end. Access through the end plugs is provided through threaded holes for fluid inflow/outflow and electrical connection to the MRI probe. The type of MRI probe may vary depending on the style of magnet employed. In the case of superconducting magnets, a birdcage or saddle coil is suitable. A conventional RF shield is not required as the outer case performs this function. The probe is tuned and matched with an external tuning box. The RF probe assembly is sealed with a high strength epoxy [18] impermeable to water.

The core holder is pressurized by introducing a non-proton containing fluid (e.g., fluorinated oils) into the holder through external connection using a hydraulic pump. In this work nitrogen gas was chosen to pressurize the core holder. Radial pressure is exerted on the sample through the containment sleeve by pressurizing the internal space. The containment sleeve isolates the sample from the pressurizing fluid. The sleeve, the pressurizing fluid, and all components inside the metal case are chosen to minimize ^{1}H background signal.

According to Fig. 1b, a prototype core holder was manufactured using non-magnetic Nitronic 60 stainless steel [16], as shown in Fig. 1c. The cylindrical steel cell has an outside diameter of 7.6 cm, an inside diameter of 5.1 cm, and a length of 30.5 cm. An 8-rung birdcage RF coil was embedded in epoxy, yielding a cylindrical sample space 3.2 cm in diameter and 7.6 cm in length. The RF probe is connected by a rigid co-axial cable to an external tune and match circuit.

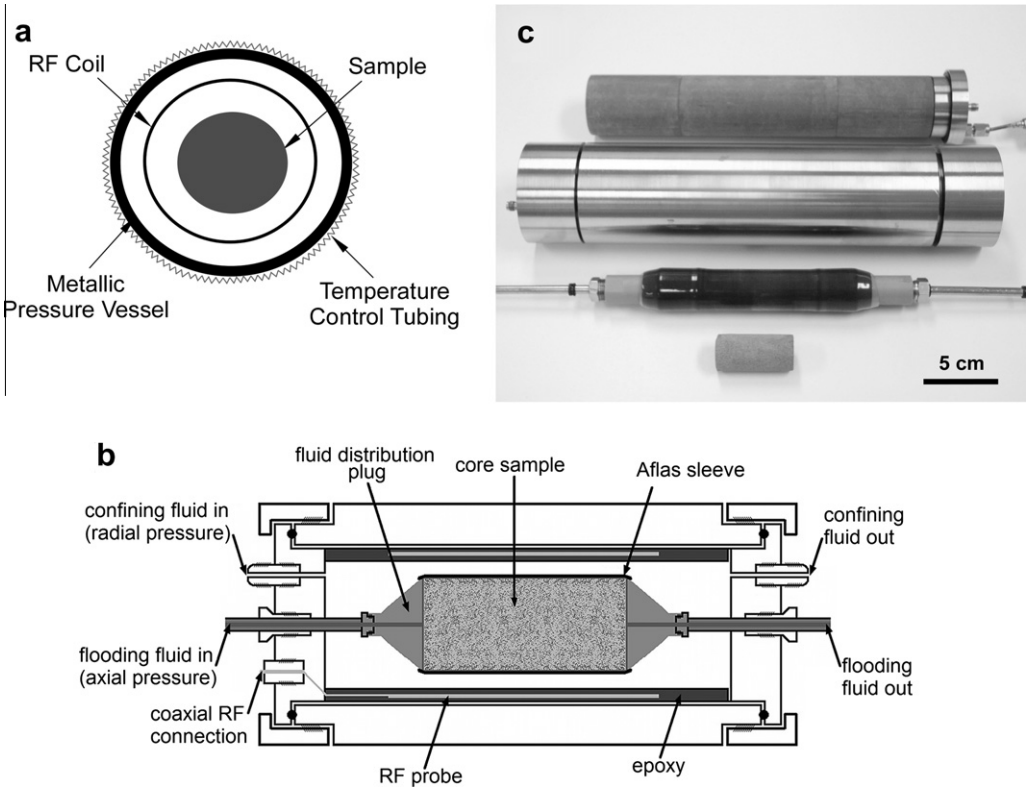

Fig. 1. MRI of high pressure systems in metallic vessels. (a) End on schematic of MRI compatible metallic pressure vessels. The RF coil is integrated inside the metallic vessel for MR imaging of macroscopic systems under variable pressure and temperature. (b) Cross-sectional diagram of a metallic core holder embodying the principles of (a) for the study of rock core samples. (c) Photo of a core holder prototype fabricated using Nitronic 60 non-magnetic stainless steel. The core plug sample, bottom, is held by heat shrink tubing and a liner to make a connection to the inlet and outlet flow pipe, second from bottom. The encapsulated sample is positioned inside the RF probe, top. The RF probe is an 8-rung birdcage probe embedded in rigid epoxy. The entire assembly goes into the Nitronic 60 non-magnetic stainless steel vessel, second from top. The vessel is sealed at the ends by screw on end pieces.

Table 1
Physical properties relevant to MRI compatible pressure vessels.

Material[a]	Yield strength (MPa)	Thermal conductivity (W/mK)	Electrical conductivity ($\times 10^6$ S/m)	Machinability[c] scale (1–5)	Cost scale (1–5)
Aluminum	200	150	37.7	xxxxx	xxx
Brass	100	109	15.6	xxxxx	xxx
Copper	60	401	58.8	xxxxx	xx
Nitronic 60 stainless steel	400	16	1.39	xxx	xxxx
Titanium	400	22	2.56	xxxx	xxxxx
PEEK polymer	96	0.25	–[b]	xxxx	xxxx

[a] Material properties are reproduced from Refs. [16,17].
[b] PEEK is an insulator with minimal conductivity.
[c] A high rating indicates ease of machining.

3. Results and discussion

3.1. Temperature control

Operation at variable pressure and temperature are principal requirements for pressure vessels. Temperature control is traditionally problematic in MR/MRI since MR observable fluids cannot be readily employed. Commercial solutions [9], such as those from Temco [10], involve circulating a fluorinated oil under high pressure through the pressure sleeve. This method involves regulating both the temperature and pressure of the fluid that is applying the radial confining pressure to the sample, which is a very complicated and expensive solution.

One may however readily exploit the high thermal conductivity of metals forming the fabric of the pressure vessel for temperature control. The high thermal conductivity of metals permits the circulation of temperature regulated water through tubing in contact with the exterior of the metal pressure vessel to control the temperature in the interior sample space. Water is a natural choice given the high thermal capacity of water and ease of handing water flow. One need not be concerned about MR/MRI detection of the external water by the RF probe since the metallic vessel acts as an RF shield. This temperature control strategy is simple, robust and is advantageous because it separates temperature control from pressure regulation. This method is not possible with conventional MRI-compatible core holders made of polymers with low thermal conductivities.

The Nitronic 60 non-magnetic stainless steel core holder was tested for temperature control. The temperature in the sample space as a function of the external temperature was measured with a thermocouple attached in the sample space. To reach a steady state sample space temperature of 50 °C from room temperature required 45 min in initial studies.

3.2. RF B_1 field

Placement of the RF coil in close proximity to the sample space maximizes the probe sensitivity. The principle of reciprocity suggests that maximizing RF coil sensitivity requires maximizing the RF magnetic field B_1 per unit current in the sample space [19]. The B_1 field (at the centre of the coil) per unit current is inversely proportional to the size of the probe coil [20]. For example, Eq. (2) describes the magnetic field at the centre of the current loop for a circular flat coil with radius of R

$$B = \frac{\mu_0 I}{2R} \tag{2}$$

where μ_0 denotes the vacuum magnetic permeability and I is the total current in the loop. The proposed RF probe design, inside the pressure cell, provides at least a doubled sensitivity compared to conventional MRI compatible pressure vessels simply by placing the RF coil inside the pressure vessel rather than outside.

Locating the RF probe inside the metallic pressure vessel improves the experiment sensitivity by increasing signal as described above, and by decreasing noise. To illustrate the efficacy of the EMI shielding of the metallic pressure vessel, the background noise level was measured for three cases inside the magnet: the birdcage probe without any RF shielding, the probe with a conventional copper RF shield, and the probe enclosed within the steel core holder. The spectrometer was set to a frequency of 94.25 MHz. This is not the 2.4 T Larmor frequency, but is a similar frequency which the probe tuning can reach for all three cases. The background noise standard deviation for the above three cases had relative ratios of 11.0, 1.7, and 1 respectively. Not surprisingly the metallic core holder functions very well as an RF shield blocking RF interference from the surroundings. The frequency of the probe shifted from 99.0 MHz to 84.3 MHz when the probe was removed from the stainless steel core holder. The probe quality factor Q however had the same value, 120, with the metal vessel (resonant frequency 99.0 MHz) and without the metal vessel (frequency 84.3 MHz). The metal vessel RF shield increases the total inductance of the probe circuit compared to the no metal case. This decreases the quality factor Q. When tuned to a common resonant frequency of 94 MHz, the Q was 110 in the absence of the metal vessel but 93 with the vessel present. The resonant frequency of the probe shifts by less than 0.2 MHz for a temperature range from 15 °C to 50 °C and does not change under moderate pressure.

3.3. Static B_0 field

The static B_0 field homogeneity is an important magnetic resonance property. It is well known that the magnetic field inside a cylindrical NMR tube is uniform regardless of whether the polarizing magnet field is axial or transverse [21,22]. This property is essential to high-resolution NMR. Assume that an annular cylinder of relative magnetic permeability μ_2, with the inner radius a and outer radius b, is embedded in a uniform environment of relative permeability μ_1. With the applied magnetic field B_0 transverse to the longitudinal axis of the cylindrical tube, the magnetic field in the interior of the tube is given by the following equation:

$$B(r) = \frac{4\mu_1\mu_2}{(\mu_2+\mu_1)^2 - (a/b)^2(\mu_2-\mu_1)^2} B_0 \tag{3}$$

The magnetic field in the interior of the tube is uniform [23] as Eq. (3) has no r dependence. The field exterior to the tube depends on r and is inhomogeneous. With the applied magnetic field B_0 parallel to the longitudinal axis of the tube, the magnetic field in the interior of the tube is uniform while the field exterior to the tube is also homogeneous [23]. One could consider the metallic pressure vessels proposed to be oversize NMR tubes.

Inside a realistic metallic core holder, field distortion may arise from imperfect alignment of the cell and the effect of vessel components such as metal end plates. The magnetic field inside the sample space was experimentally measured, by MRI, for the

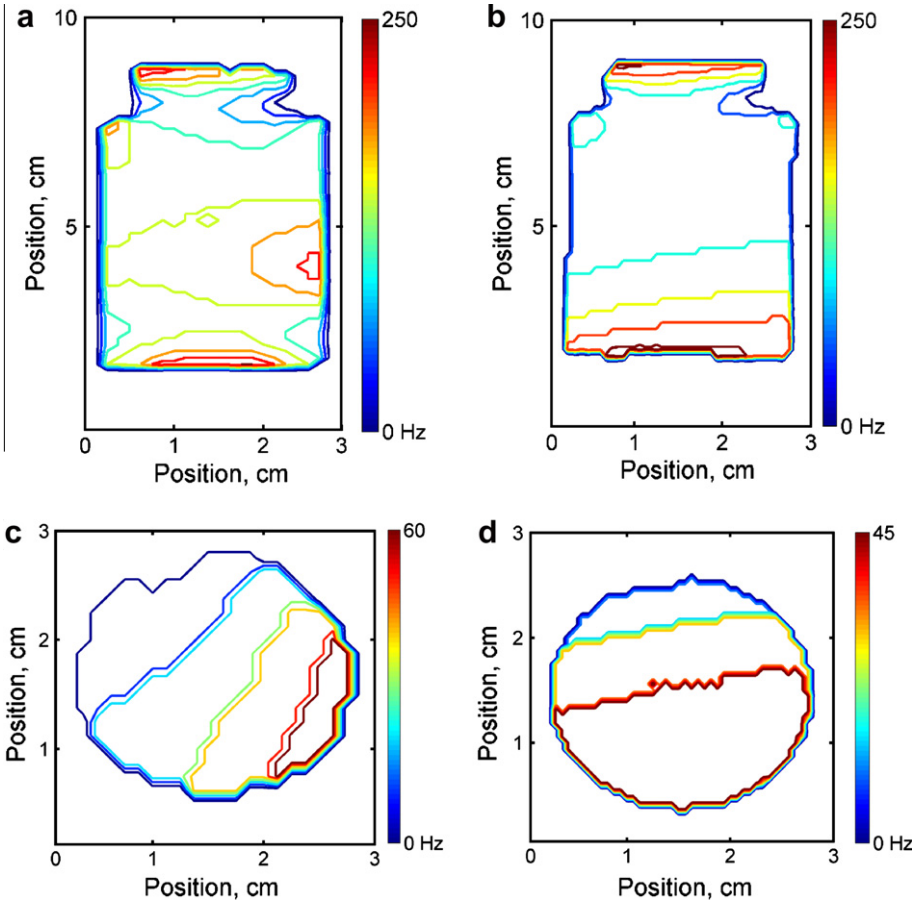

Fig. 2. Measurement of the static field distribution inside the Nitronic stainless steel core holder in comparison to the case of no metal vessel. Field offset map $\Delta B_0(r)$ in the central longitudinal *ZX* plane for (a) the steel core holder and (b) the conventional Birdcage probe. (c and d) Field offset maps in the central transverse *XY* plane for the steel core holder and the conventional Birdcage probe respectively. Each contour line corresponds to a spectral resolution of 18 Hz (0.18 ppm). The metal enclosure does not introduce significant B_0 field inhomogeneity in the sample space.

Nitronic 60 stainless steel core holder and compared to a similar volume in the absence of the vessel. A cylindrical bottle of doped water was measured, length 7.3 cm and inside diameter 2.6 cm, for both cases. Simple first-order shimming was applied using *x*, *y*, and *z* gradient coils in each case to homogenize the field in the sample space. Inside the cell the bulk frequency spectrum is slightly broadened compared to the case without the cell. The Lorentzian linewidth increased from 45 Hz (0.45 ppm) without the cell to 60 Hz (0.6 ppm) with the cell.

Magnetic field $B_0(r)$ maps were acquired in each case employing pure phase encode 3D spin echo measurements with digitization of the echo. Fig. 2 shows cross sections of the 3D field offset $\Delta B_0(r)$ map in (*a*–*b*) longitudinal *ZX* planes and (*c*–*d*) transverse *XY* planes. In the longitudinal plane inside the cell, fields are largely uniform within 0.3 ppm across the axial sample space over 5 cm, as shown in Fig. 2a, except at the two ends of the bottle. Field inhomogeneity at the ends of the sample bottle arises from magnetic susceptibility differences between air, glass, and water. In the transverse plane, inside the cell, the field in Fig. 2c showed a slight gradient of 20 Hz/cm in contrast to the field gradient of 14 Hz/cm observed in Fig. 2d with a conventional probe setup. These field gradients could be easily removed with more careful shimming. The 3D spatially resolved field maps agree with the bulk FID measurements. The metal vessel does not create significant B_0 field inhomogeneity in the sample space. Residual B_0 field inhomogeneities are driven by inhomogeneities in the main field, not due to the metal vessel.

3.4. Dynamic B_0 field

Switched magnetic field gradients are the essential basis of spatial encoding and motion sensitization in modern MR/MRI. As the magnetic field gradient switches, eddy currents will circulate in metals, and may distort the desired magnetic field in the sample space. This may be problematic for MRI pulse sequences demanding high gradient fidelity such as EPI and Spiral scanning [13]. We have employed the magnetic field gradient waveform monitor (MFGM) method [24] to successfully address the eddy current problem associated with imaging inside highly conductive metal (aluminum) structures [11].

Induced eddy currents in the cylindrical metal vessel decay exponentially with a time constant that is proportional to the electrical conductivity of the metal as described by the following equation [11,25]:

$$\tau = K\sigma\mu\Gamma \tag{4}$$

where τ is the eddy current time constant, σ and μ are the electrical conductivity and magnetic permeability, while K is a constant. Γ represents a geometric factor. Illustrated in Table 1, a stainless steel vessel compared to aluminum reduces eddy current time constants by a factor of almost 30. Fig. 3a shows a gradient waveform measured for the steel core holder with the MFGM method [24]. The input was a rectangular pulse of duration 4 ms. The gradient rise time was 0.5 ms from 10% to 90%. By comparison, the aluminum vessel

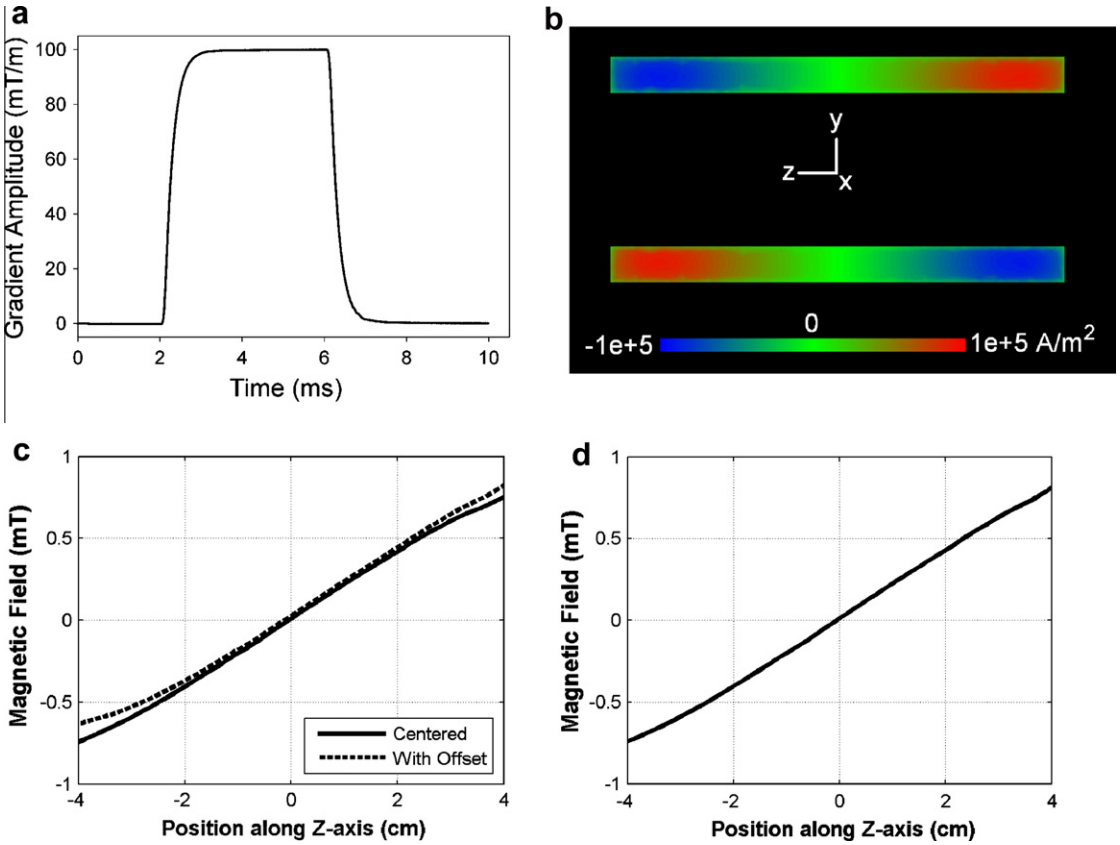

Fig. 3. Measurement and simulation of the G_z gradient inside a non-magnetic stainless steel vessel. (a) Gradient waveform measurement inside the steel core holder of Fig. 1c. The gradient had a rise time of 0.5 ms from 10% to 90%. (b–d) Simulation of eddy current effects for a cylindrical stainless steel vessel with a length of 15.2 cm, an outside diameter of 7.6 cm and a wall thickness of 1.3 cm. (b) Longitudinal cross sectional representation of the eddy current density within the vessel 200 μs after switching the gradient off. (c) The magnetic field caused by eddy currents in (b) at the same time along the central axis of the vessel. The two lines correspond to the cell centered inside the gradient coil and the cell offset 1 cm with respect to the gradient origin respectively. (d) The same field as that in (c) except for a cell with a stainless steel end plate on the right side.

with a similar geometry had a gradient rise time of 10 ms [11]. The natural rise time of the z gradient was 80 μs.

The relatively low electrical conductivity of non-magnetic stainless steel is also desirable for travelling wave NMR/MRI [26] where a stainless-steel mesh enclosing the human body was employed as a radio-frequency screen to guide travelling waves at the NMR frequency.

As part of this work we have simulated eddy currents and their induced magnetic fields for various metallic pressure vessels. Simulation permits rapid survey of vessel parameters such as metal type and geometry, which would not be easily accomplished experimentally due to the associated material and machining costs. Gradient waveforms were simulated in this work for both Nitronic 60 stainless steel and aluminum cells (not shown) with appropriate geometries for comparison with MFGM waveform measurements. Simulation and experiments agreed very well. The difference between gradient rise times measured experimentally and determined through simulation was less than 5%.

For simulation of the G_z gradient, a cylindrical Nitronic 60 stainless steel cell was centered within the linear range of a simulated 'Maxwell' pair magnetic field gradient coil. The cell had a length of 15.2 cm with the outside diameter and wall thickness identical to the practical core holder of Fig. 1c. Fig. 3b shows the instantaneous eddy current density distribution at 200 μs after a gradient pulse G_z, 2 ms in duration and 40 mT/m in amplitude, is switched off. The eddy current distribution shows a rigorous antisymmetry with respect to the gradient origin as expected. The solid line in Fig. 3c shows the magnetic field, produced by eddy currents in Fig. 3b, along the central axis of the cell. The field has a near linear gradient over 5 cm in the middle of the sample space.

The dashed line shows the same field but with the cell offset −1 cm along Z. It shows that a spatially constant ΔB_0 field was created with the cell displaced from the gradient origin. This agreed with our previous measurements [11], which indicated that a spatially constant $\Delta B_0(t)$ was minimized and thus negligible if the cell was centered inside the gradient coil. Fig. 3d shows the same field as the solid line in Fig. 3c except that the cell has an end plate on the right side with a thickness of 1.3 cm. The presence of an end plate improves the linear range of the gradient field which suggests that our next generation core holders may be reduced in length.

The G_x and G_y gradient simulations (not shown) reveal essentially similar features to the G_z gradient simulation. Our previous gradient waveform measurements and associated image correction [11] also suggested that, with a cylindrical metallic cell closed and centered inside the gradient coil, eddy currents in response to gradient switches in all three directions mainly result in an additional magnetic field gradient in the corresponding direction that can be readily corrected using measured gradient waveforms. The phenomenon is similar to the method of mirror charges in electrostatics [27]. Eddy current behavior in cylindrical metal vessels favors high pressure MRI with metallic vessels.

3.5. Imaging

As a simple example of the non-magnetic Nitronic 60 stainless steel core holder, water flooding in a sandstone rock core was monitored with MRI. Fig. 3a shows that the magnetic field gradient pulse stabilizes less than 1.5 ms after a switch in a stainless steel core holder. For quantitative centric scan SPRITE imaging [28] k-space samples are acquired at the end of each gradient step with a repetition time of 1–2 ms. The k-space acquisition will not be altered by eddy current effects with a repetition time of 2 ms, and therefore centric scan SPRITE does not necessitate eddy current corrections as it was required for imaging inside an aluminum vessel [11].

The two dimensional centric scan SPRITE imaging modality, Spiral SPRITE with four interleaves [28], was employed for test imaging. As shown in Fig. 4, water was driven through a dry Berea sandstone from right to left. The confining pressure and the temperature were set to 20 bar and 50 °C respectively. During the flooding experiment, 2D images were acquired at intervals of 43 s. Acquisition time per 2D longitudinal *ZY* image was 43 s with four signal averages. After 40 min of imbibition the rock was fully saturated. Background signal, from the epoxy that supports the RF

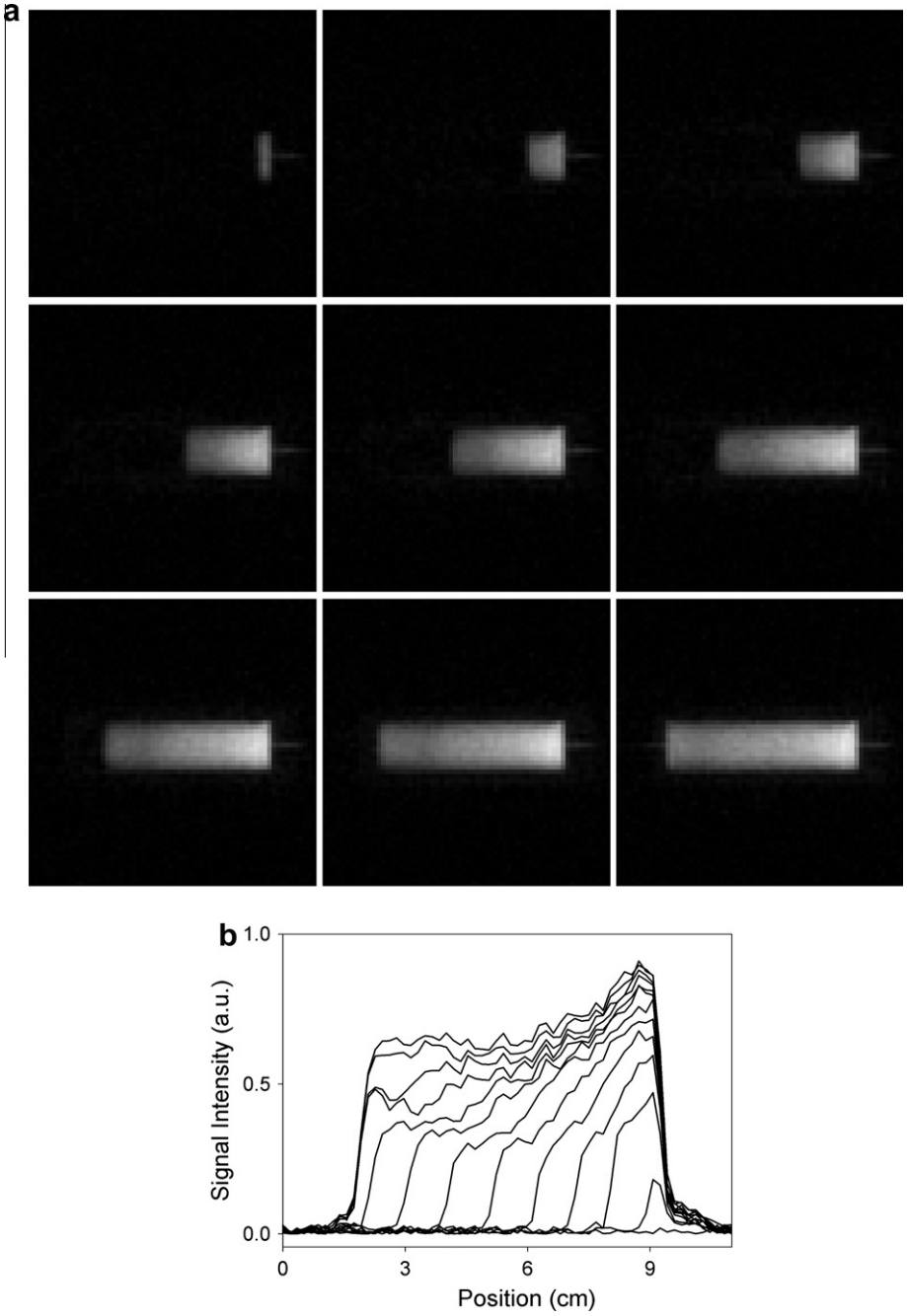

Fig. 4. MRI monitoring of water flooding a Berea sandstone core sample in the steel core holder under moderate pressure and temperature. Water migrated through the dry rock from right to left. 2D *ZX* image were acquired at intervals of 43 s. The rock, 25 mm in diameter and 75 mm in length, saturated in 40 min. (a) Nine of the 2D images, at intervals of 3.6 min, acquired during water penetration. The field of view (FOV) was 12 cm * 12 cm. (b) 1D profiles extracted from the center line of the 2D images at intervals of 3.6 min. Note progression of the wetting front through the porous sample. Note also increased image intensity as a function of time behind the wetting front.

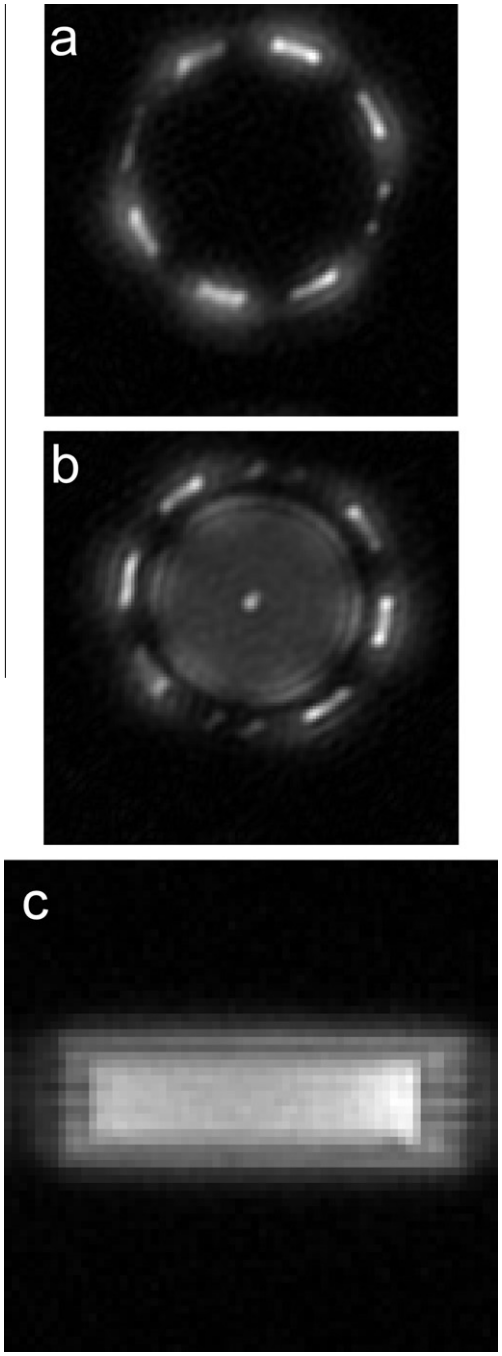

Fig. 5. Background signal from polymer materials in Fig. 1b. (a) 2D image of the empty probe in the transverse plane (XY). The image reflects the B_1 field enhancement around the Birdcage RF probe struts. (b) The same transverse 2D image with the water saturated Berea rock in place. The water inside the rock had a short transverse MR lifetime of 90 μs in the 2.4 T magnetic field. (c) Side view of the 2D image of the same Berea sample.

probe, has been removed by the subtraction of an empty probe image.

4. Conclusion

We have proposed high pressure MRI measurement using non-magnetic metallic vessels in the context of a rock core holder. Compared to conventional MRI core holders and pressure vessels, the proposed metallic pressure vessels permit much more efficient temperature control and optimized sensitivity. Magnetic resonance properties associated with the metallic pressure vessel have been investigated both experimentally and through simulation. The magnetic field inside metallic pressure vessels is largely homogeneous. Eddy currents are dramatically reduced using stainless steel, with its relatively low electrical conductivity compared to other metals. Quantitative centric scan SPRITE imaging does not require eddy current correction.

Eddy currents mainly distort the gradient waveform inside the sample space but do not preclude high quality MRI. Appropriate eddy current correction schemes such as the MFGM method may permit the full array of gradient related MR methods to be employed in conjunction with these vessels for both spatial and motion encoding. Quantitative imaging of water flooding a rock core plug in a stainless steel core holder under moderate pressure and temperature shows the potential of this methodology. MRI compatible metallic pressure vessels enable macroscopic systems at high pressure and variable temperature to be monitored by MRI.

5. Experimental

5.1. Experimental details

The core holder was centered along the B_0/G_z axis inside a microimaging gradient set in a Nalorac (Martinez, CA) 2.4 T 32 cm horizontal bore superconducting magnet. The gradient set was driven by a Techron (Elkhart, IN) 8710 amplifier with a Tecmag (Houston, TX) Apollo console.

In the magnetic field $B_0(r)$ mapping experiment, spin echoes with phase encoding in all three spatial dimensions were acquired and Fourier transformed to obtain the spatially resolved frequency spectra. The echo time (TE) between the 90° excitation RF pulse and the echo centre was 10 ms. This ensured that phase encoding gradient pulses of 1 ms duration fully decayed before the 180° refocusing RF pulse. The image matrix was $48 * 48 * 64$ with a spatial resolution of $0.6\,\text{mm}(x) * 0.6\,\text{mm}(y) * 1.6\,\text{mm}(z)$. The 112 time domain data points with a dwell time of 500 μs were acquired for each echo, producing a spectral resolution of 18 Hz (0.18 ppm). The total measurement time for a 3D $B_0(r)$ map was 11 h with one signal average.

In water flooding experiments the water flow rate was 0.3 ml per minute. Acquisition time per $64 * 64$ 2D image was 43 s with four signal averages. The RF pulse for Spiral SPRITE imaging was 12° with a duration 2 μs. The encoding time t_p was 140 μs with a repetition time (TR) of 2 ms. The maximum gradient strength was 120 mT/m with a field of view (FOV) $12\,\text{cm} * 12\,\text{cm}$. A time interval of 1 s was allowed between Spiral SPRITE interleaves and also between each scan.

Simulation was undertaken with Computer Simulation Technology (CST) (Framingham, MA) Electromagnetics (EM) Studio.

5.2. Background MR signal

Background MR signal arises from the polymer materials inside the pressure vessel. A G10 glass reinforced fiberglass tube (McMaster-Carr) was machined with space for the birdcage RF probe. That space with the coil and rigid co-axial cable in place was then filled with West System epoxy (Bay City, MI) to make a solid cylinder. It is expected that the strength of the background signal will increase with temperature, since the T_2^* of polymers are generally longer at elevated temperatures [18].

Fig. 5a shows a 2D image in the transverse plane (*XY*) with the empty RF probe. These signals are from epoxy in proximity to the eight rungs of the birdcage RF probe, where RF B_1 field is enhanced [20]. The local image intensity reflects the current distribution on

the eight rungs of the birdcage. Most (80%) of the background polymer signal has a short lifetime of less than 100 μs, which will not be problematic for imaging of porous media in the low magnetic field since the fluid in porous media such as a rock core usually has MR lifetimes of a few hundreds of microseconds [29].

Fig. 5b shows the same transverse image with the water saturated Berea rock core present. At 2.4 T, the water in the rock core has a significantly decreased MR lifetime (T_2^*) of about 90 μs. The water signal in the rock core is of similar intensity compared to the epoxy signal. However the epoxy is physically separate from the sample space and can be distinguished in an image. At the circular edge of the rock, core image signal is slightly enhanced due to background signal from the Aflas sleeve in Fig. 1b housing the rock. Note the bright spot at the center of the rock core image. This is from water in the inlet/outlet tubing as seen in the side view image Fig. 5c.

Acknowledgments

B.J.B. thanks the Canada Chairs program for a Research Chair in MRI of Materials (2009–2016), NSERC of Canada for a Discovery grant, and Conoco Philips. We thank many for their assistance and suggestions: IIT undergraduate K. Adusumilli sponsored by the MITACS program, Drs. I. Mastikhin and B. Newling, as well as M. Olive and B. Titus.

References

[1] B. Benedek, M.J. Purcell, Nuclear magnetic resonance in liquids under high pressure, Chem. Phys. 22 (1954) 2003–2012.
[2] J. Jonas, Nuclear magnetic resonance at high pressure, Science 216 (1982) 1179–1184.
[3] J.D. Grunwaldt, R. Wandeler, A. Baiker, Supercritical fluids in catalysis: opportunities of in situ spectroscopic studies and monitoring phase behavior, Catal. Rev. 45 (2003) 1–96.
[4] R.J. Angel, N.L. Ross, F. Seifert, T.F. Fliervoet, Structural characterization of pentacoordinate silicon in a calcium silicate, Nature 384 (1996) 441–444.
[5] I.T. Horvath, J.M. Miuar, NMR under high gas pressure, Chem. Rev. 91 (1991) 1339–1351.
[6] S.K. Lee, K. Mibe, Y.W. Fei, G.D. Cody, B.O. Mysen, Structure of B_2O_3 glass at high pressure: a ^{11}B solid-state NMR study, Phys. Rev. Lett. 94 (2005) 165507.
[7] K.J. Thurecht, D.J.T. Hill, A.K. Whittaker, Equilibrium swelling measurements of network and semicrystalline polymers in supercritical carbon dioxide using high-pressure NMR, Macromolecules 38 (2005) 3731–3737.
[8] R.H. Morris, M. Bencsik, N. Nestle, P. Galvosas, D. Fairhurst, A. Vangala, Y. Perrie, G. McHale, Robust spatially resolved pressure measurements using MRI with novel buoyant advection-free preparations of stable microbubbles in polysaccharide gels, J. Magn. Reson. 193 (2008) 159–167.
[9] B.A. Baldwin, J. Stevens, J.J. Howard, A. Graue, B. Kvamme, E. Aspenes, G. Ersland, J. Huseb, D.R. Zornes, Using magnetic resonance imaging to monitor CH_4 hydrate formation and spontaneous conversion of CH_4 hydrate to CO_2 hydrate in porous media, Magn. Reson. Imaging 27 (2009) 720–726.
[10] L. Li, Q. Chen, A.E. Marble, L. Romero-Zerón, B. Newling, B.J. Balcom, Flow imaging of fluids in porous media by magnetization prepared centric-scan SPRITE, J. Magn. Reson. 197 (2009) 1–8.
[11] H. Han, D. Green, M. Ouellette, R. MacGregor, B.J. Balcom, Non-Cartesian sampled centric scan SPRITE imaging with magnetic field gradient and $B_0(t)$ field measurements for MRI in the vicinity of metal structures, J. Magn. Reson. 206 (2010) 97–104.
[12] R.E. Gerald, R.J. Klingler, J.W. Rathke, G. Sandi, K. Woelk, In situ imaging of charge carriers in an electrochemical cell, in: P. Blümler, B. Blümich, R. Botto, E. Fukushima (Eds.), Spatially Resolved Magnetic Resonance, Wiley-VCH, New York, 1998, pp. 111–119.
[13] M.A. Bernstein, K.F. King, X.J. Zhou, Handbook of MRI pulse sequences, Elsevier Academic Press, Burlington, 2004.
[14] B. Blumich, NMR Imaging of Materials, Oxford University Press, Oxford, 2000.
[15] E.F. Megyesy, Pressure Vessel Handbook, PV Publishing Inc., Oklahoma City, 2008.
[16] J.R. Davis, ASM Handbook Committee, Metals Handbook, ASM International, Materials Park, Ohio, 2008.
[17] M.F. Ashby, D.R.H. Jones, Engineering Materials, Pergamon Press, Oxford, UK, 1992.
[18] B. MacMillan, M. Halse, M. Schneider, L. Fardy, Y.H. Chui, B.J. Balcom, Magnetic resonance imaging of rigid polymers at elevated temperatures with SPRITE, Appl. Magn. Reson. 22 (2002) 247–256.
[19] D.I. Hoult, The principle of reciprocity in signal strength calculations – a mathematical guide, Concepts Magn. Reson. 12 (2000) 173–187.
[20] J. Mispelter, M. Lupu, A. Briquet, NMR Probeheads for Biophysical and Biomedical Experiments Theoretical Principles & Practical Guidelines, Imperial College Press, London, 2006.
[21] D.T. Edmonds, Theory of resonance in magnetically inhomogeneous specimens and some useful calculations, J. Magn. Reson. 77 (1988) 223–232.
[22] P.T. Callaghan, Principles of Nuclear Magnetic Resonance Microscopy, Oxford University Press, Oxford, 1991.
[23] T.D.W. Claridge, High-Resolution NMR Techniques in Organic Chemistry, Elsevier, Oxford, 1999.
[24] H. Han, R. MacGregor, B.J. Balcom, Pure phase encode magnetic field gradient monitor, J. Magn. Reson. 201 (2009) 212–217.
[25] R.L. Stoll, The Analysis of Eddy Currents, Clarendon Press, Oxford, 1974.
[26] D.O. Brunner, N.D. Zanche, J. Fröhlich, J. Paska, K.P. Pruessmann, Travelling-wave nuclear magnetic resonance, Nature 457 (2009) 994–998.
[27] D.J. Griffiths, Introduction to Electrodynamics, Prentice-Hall, Upper Saddle River, 1999.
[28] M. Halse, J. Rioux, S. Romanzetti, J. Kaffanke, B. MacMillan, I. Mastikhin, N.J. Shah, E. Aubanel, B.J. Balcom, Centric scan SPRITE magnetic resonance imaging: optimization of SNR, resolution and relaxation time mapping, J. Magn. Reson. 169 (2004) 102–117.
[29] Q. Chen, A.E. Marble, B.G. Colpitts, B.J. Balcom, The internal magnetic field distribution, and single exponential magnetic resonance free induction decay, in rocks, J. Magn. Reson. 175 (2005) 300–308.